RESEARCH PAPER

Imaging properties of Fe_3O_4@Au and Fe_3O_4@Bi hybrid nanocomposites as contrast agents in spectral X-ray computed tomography: A Monte Carlo simulation study

Maryam Sadeghian [1,2], *Asghar Mesbahi* [3*]

[1]*Medical Radiation Sciences Research Team, Tabriz University of Medical Sciences, Tabriz, Iran*
[2]*Medical Physics Department, Medical School, Tabriz University of Medical Sciences, Tabriz, Iran*
[3]*Molecular Medicine Research Center, Tabriz University of Medical Sciences, Tabriz, Iran*

ABSTRACT

Objective(s): In this paper, we evaluated some imaging properties of Fe_3O_4@Au and Fe_3O_4@Bi hybrid nanocomposites as contrast agents in spectral CT. For this purpose, we simulated a spectral CT scanner with photon-counting detectors (PCDs) in 6 energy bins by a Monte Carlo simulator.

Materials and Methods: A cylindrical phantom was designed with a diameter of 8 cm and a height of 10 cm. Fe_3O_4@Au and Fe_3O_4@Bi hybrid nanocomposites were designed as a core-shell with a diameter of 80 nm. Simulation results were utilized to reconstruct cross-sectional images through the filtered back-projection (FBP) algorithm in MATLAB software. Signal intensity and contrast to noise ratio (CNR) of tested contrast agents were calculated in spectral CT images.

Results: The results indicated a comparable image quality for Fe_3O_4@Au and Fe_3O_4@Bi hybrid nanocomposites at different energy bins. However, in the energy range of 80 to 120 keV (bin 4 and 5), the difference in signal intensity and CNR between these two nanocomposites increased. The maximum signal intensity and CNR for Fe_3O_4@Au and Fe_3O_4@Bi were acquired at the highest concentration. The maximum signal intensity for Fe_3O_4@Au was 144±10 (HU) in the 4th energy bin and for Fe_3O_4@Bi 162±19 (HU) in the 5th energy bin. Besides, the maximum CNRs of 74±6 and 67.5±9 for Fe_3O_4@Au in bin 4, while for Fe_3O_4@Bi in bin 5 were obtained respectively.

Conclusion: Based on our results, Fe_3O_4@Au and Fe_3O_4@Bi hybrid nanocomposites have provided promising results as contrast agents in spectral CT. Fe_3O_4@Bi nanocomposites are recommended due to their lower price and availability.

Keywords: *Bismuth nanoparticles; Gold nanoparticles; Hybrid nanocomposites; Iron oxide nanoparticles; Spectral computed tomography*

How to cite this article
Sadeghian M, Mesbahi A. Imaging properties of Fe_3O_4@Au and Fe_3O_4@Bi hybrid nanocomposites as contrast agents in spectral X-ray computed tomography: A Monte Carlo simulation study. Nanomed J. 2021; 8(3): 220-228. DOI: 10.22038/nmj.2021.57220.1588

INTRODUCTION

Medical imaging modalities including magnetic resonance imaging (MRI), X-ray computed tomography (XCT), positron emission tomography (PET), and single photon emission computed tomography (SPECT) are essential components in the diagnosis and treatment of diseases [1]. X-ray CT is the most used imaging modality, due to its availability, economical, high spatial resolution, and faster image reconstruction [2, 3]. Spectral XCT is a new form of CT that has emerged in recent years and can be employed for clinical and preclinical applications [4, 5]. Spectral CT scanner applies a standard polychromatic X-ray source and photon-counting detectors (PCDs) [6, 7]. Conventional CT scanners use energy integrating detectors (EIDs) [8]. The EID detects signals that are equivalent to the total energy of the accumulated photons in each pixel, without specific information about the individual photon. On the other hand, PCDs have the ability to evaluate spectral information from a polyenergetic X-ray spectrum due to their adjustable energy

* *Corresponding Author Email: amesbahi2010@gmail.com*
Note. This manuscript was submitted on April 21, 2021; approved on May 25, 2021

thresholds [9-11]. Also, PCDs can record different linear attenuation coefficient measurements for the identical object at distinct energies [6, 12-14]. Spectral CT systems have several advantages over conventional CT systems including lower noise, enhanced contrast to noise ratio (CNR) and better diagnosis for a diversity of diseases [4, 8, 15, 16]. In many CT imaging protocols, a contrast agent may be used to enhance the distinction between two types of tissue and to evaluate the function of cells or tissues [7]. Iodine-based contrast agents are widely applied as contrast agents in CT imaging. Although iodine-based contrast agents provide high contrast resolution, they may impair organs function [17-19]. Therefore, in past decades; many studies have been carried out to discover a suitable alternative to iodine-based contrast agents in CT [4, 6, 12, 18, 20]. Significant studies have been performed using nanoparticles based on elements, for instance, gold, gadolinium, bismuth, silver, tantalum, and others as contrast agents for CT [21-27]. The results of these studies demonstrate that nanoparticles as contrast agents improve imaging quality and have targeting ability compared to conventional contrast agents as well as longer circulation time in in-vivo conditions [10, 28-32]. Another feature of nanoparticles is the facility of synthesizing different imaging contrast agents in one hybrid material, which provides an efficient platform for multimodal imaging such as MR/CT, PET/CT, SPECT/CT, and MR/fluorescence [33, 34]. Hybrid structures are more attractive than their single-component samples because they have the potential to merge the unique attributes of two nanomaterials in one existence [33]. Hybrid nanostructures have various physicochemical properties that are therefore widely used in nanomedicine, especially medical imaging. In hybrid structures used in medical imaging, iron oxide nanoparticles are valuable components [35]. Iron oxide nanoparticles can be used as T2-weighted contrast agents in MRI due to their superparamagnetic behavior. These magnetic nanoparticles in combination with metal nanoparticles such as gold, platinum, bismuth, or silver can be utilized as dual contrast agents in XCT and MRI [36-38]. Today, it is possible to synthesize hybrid structures with different architectures such as dumbbell, core-shell, core-hollow shell, nanoflower, etc [39]. Wang et al, reported that gold-coated iron oxide core-shell nanoparticles (Fe_3O_4@Au nanoparticles) exhibit higher chemical stability by safeguarding the core from corrosion and oxidation, as well as they show better biocompatibility and affinity through amine/thiol terminal groups on the gold (Au) surface [40].

The previous studies indicated the potential uses of hybrid nanocomposites in CT and MRI. However, to the best of our knowledge, no study has been conducted on the application of these novel hybrid contrast agents in spectral CT. For the first time, we evaluated the properties of these two nanocomposites in spectral CT using a validated Monte-Carlo (MC) model. The effect of concentration, the energy of photons, and nanocomposite composition was studied using a quantitative approach in which signal intensity and contrast to noise ratio (CNRs) were compared.

MATERIALS AND METHODS

Monte carlo simulation of CT scanner

The CT spectral scanner was simulated via Monte-Carlo simulation. The Monte-Carlo simulation was performed using MCNPX code version 2.6.0 [41]. For this simulation, a GE 64-slice (LightSpeed, VCT) CT scanner (General Electric Healthcare Technologies, Waukesha, WI, USA) was applied as a model to simulate the spectral CT system. The CT scanner was designed in the form of a cylinder with a fan beam and a detector row. The geometric specifications were received from the CT scanner manufacturer. In this study, the X-ray tube was simulated as a point source that emits photons in a fan beam at an angle of 24 degrees toward detectors. The focus-to-center of rotation distance and the focus-to-detector distance in this CT scanner were 540 and 950 mm, respectively. The photon spectrum of 140 kVp was used in the scanner. The utilized X-ray spectrum was acquired by SpekCalc (version 1.0) software. The utilized photon spectrum of the scanner was displayed in Fig 1. An aluminum filter with a thickness of 3.25 mm and an additional filter of 0.1 mm copper were used to filter the X-ray beam. Also, a bowtie filter was designed in front of the X-ray source to modulate the output X-ray beam. A pair of lead collimators was simulated in front of the source on both sides of the central axis of the beam at a distance of 10 cm. Likewise, a pair of lead collimator was designed before detectors at a distance of 10 mm, which reduced scattered radiation collecting by detectors. As mentioned earlier, the simulated CT had a detector row containing 960 detector cells on an

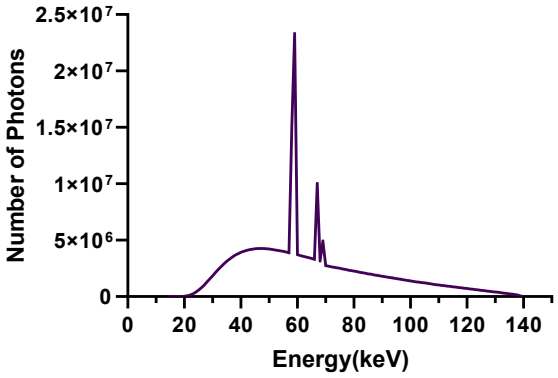

Fig 1. SpekCalc-calculated photon beam energy spectrum for 140 kVp

arc. The thickness of each detector cell in y- and z-direction was 0.625 mm and 5 mm, respectively. All detector elements had a thickness of 3 mm in the x-direction. The lattice command in MCNPX code was used to generate these detectors. The lattice command is utilized to replicate a structure, which facilitates the definition of cells in abundant numbers. The detectors of the scanner were made of cadmium telluride (CdTe). The F4 tally in MCNPX code was used to determine the average flux in the cell. The tally card is used for determining what sort of data must be gained from the Monte Carlo simulation. By using the En card in MCNPX code, 6 energy bins were defined for each detector. Each energy bin had a certain size, which was equal to 20 keV. The minimum energy measured was 20 keV and the maximum measured energy was 140 keV. Table 1 listed the energy bins and their receiving thresholds.

Phantom

In the next step, a cylindrical phantom with a radius of 4 cm and a height of 10 cm was designed in the center of the CT scanner, which was filled with water. A hole with a radius of 1.5 cm was embedded in the center of the water-filled phantom, which was the place to simulate contrast agents. Fig 2a,b shows a schematic of the simulated CT scanner and phantom.

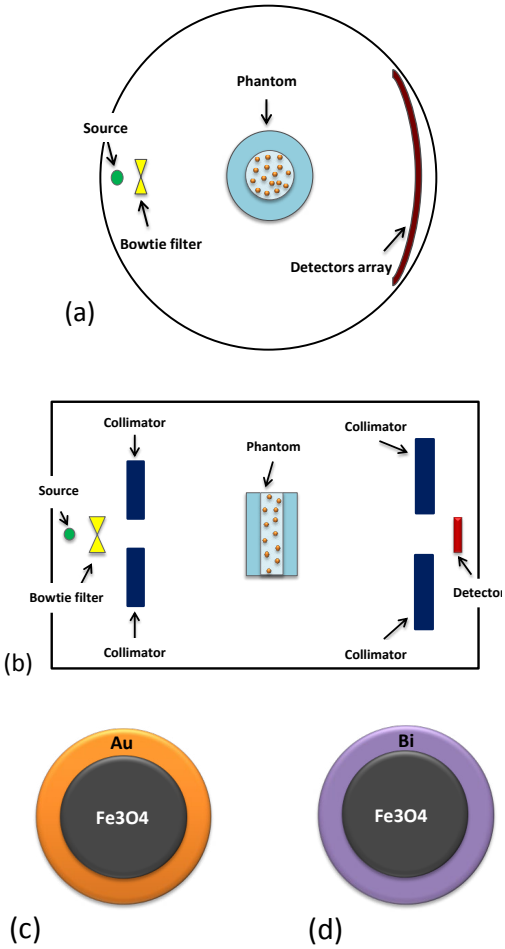

Fig 2. Schematic illustration of CT scanner and the simulated hybrid nanocomposites (a) Cross-sectional view of CT scanner (b) Top view of CT scanner (c) Fe_3O_4@Au nanoparticle (d) Fe_3O_4@Bi nanoparticle

Contrast agents

In this research, two types of hybrid nanocomposites were investigated as contrast agents including Fe_3O_4@Au and Fe_3O_4@Bi. Contrast materials were designed as core-shell. In both types of hybrid nanocomposite contrast agent, iron oxide nanoparticles (Fe_3O_4 NPs) were placed as the core, and gold (Au) or bismuth (Bi) nanoparticles as the shell were placed around

Table 1. Energy bins which were utilized in simulated detectors

Bins number	bin1	bin2	bin3	bin4	bin5	bin6
Energy range (keV)	20 to 40	40 to 60	60 to 80	80 to 100	100 to 120	120 to 140

the core. Iron oxide nanoparticle was designed with a diameter of 60 nm and covered with Au or Bi nanoparticles with a thickness of 10 nm. In consequence, the studied hybrid nanocomposites had a diameter of 80 nm. The designed hybrid nanocomposites have been presented in Fig 2c,d. Contrast agents used in this paper were simulated at four concentrations containing 0.5, 1, 2, and 4 mg/ml. To simulate a contrast agent with a specified concentration, in the first place, it was necessary to the computed density of the contrast agent. The density of the contrast agent at a given concentration was calculated as follows:

$$\frac{1}{\rho_{CM}} = \frac{\omega f_w}{\rho_w} + \frac{\omega f_i}{\rho_i} + \frac{\omega f_j}{\rho_j} \qquad (1)$$

where ρCM is the density of contrast agent and ρ_w, ρ_i, ρ_j are the densities of water, Fe_3O_4 NP, and Au or Bi nanoparticles, respectively. Besides, ωf_w, ωf_i and ωf_j are the weight fractions of water, Fe_3O_4 NP, and Au or Bi nanoparticles, respectively.

Next, the lattice command of MC was used to simulate the contrast agent within the phantom. In this way, the central hole in the phantom was divided into square cubes of defined dimensions using the lattice command. Inside each square cube, an 80 nm sphere was modeled that was a hybrid nanoparticle. The 80 nm sphere was defined as a core-shell, meaning that it had a 60 nm Fe_3O_4 sphere at its center, surrounded by a layer with a thickness of 10 nm made of gold or bismuth.

Next, the simulated CT scanner program was performed without the phantom. Data for each of the 6 energy bins were collected separately by detectors, which were called I0 for each energy bin. Then, each of the simulated programs was run in presence of a phantom with a specific contrast agent by a certain concentration, respectively. The number of photons transmitted through the phantom and received by detectors was acquired in each 6 energy bins. These acquired data were called I or intensity in each energy bin.

Each simulation program was run on a personal desktop and 2×109 histories were tracked. Also, forced collision method was utilized to reduce statistical errors of simulation results. Forced collision is one of the variance reduction methods that enhances collision in specified cells adjusted by the user. As a result, MC calculations of this study contain a statistical uncertainty of lower than 1% per cell. Next, we applied measurements I0 and I to calculate linear attenuation coefficients in a projection.

The following formula was used to calculate the linear attenuation coefficient:

$$\ln(I_0/I) = \mu x \qquad (2)$$

where μ is the linear attenuation coefficient and I_0 and I are intensities of primary photons and transmitted photons, respectively.

Image processing

In the present study, the image processing toolbox of MATLAB software was used to reconstruct images. We extracted data from MC output file and calculated Ln(I0/I). Finally, data were prepared for image processing. Using calculated Ln(I0/I) values in one projection, a sinogram matrix was constructed that has one column and 960 rows. The number of columns in the sinogram matrix indicates the number of projections and the number of rows shows the number of detectors. Then, this matrix was entered into MATLAB software as an m-file. Because our simulated phantom was symmetrical, we could replicate data of one projection for other projections. Eventually, we created a sinogram matrix with 360 columns and 960 rows. In this paper, filtered back projection (FBP) was employed to reconstruct images. For this purpose,"ifanbeam" command was used in MATLAB software. The ifanbeam is a command in MATLAB software that is utilized for image reconstruction by a device with fan-beam geometry. Linear interpolation was exploited for image reconstruction. A Hamming filter was also used to improve the quality of images. The reconstructed images contained 512 × 512 pixel arrays. In the next step, we selected a region of interest (ROI) with a size of 2500 pixels from the water-filled region of phantom and estimated the average attenuation coefficient of water in this chosen area. Then, by Equation 3, attenuation coefficients of all image pixels were transformed into Hounsfield units and images were represented in the Hounsfield scale.

$$CT\ number = \left(\frac{\mu_i - \mu_{water}}{\mu_{water}}\right) \times 1000 \qquad (3)$$

where μw, μi are the linear attenuation coefficients of water and contrast agents in CT images.

Evaluation of image quality

In this article, two parameters were used to

evaluate the quality of reconstructed images, which include signal intensity and CNR. To evaluate the signal intensity of each studied contrast agent at every energy bin, we selected an ROI with a size 1500 pixels from the middle of images. Next, we assessed the mean and standard deviation of CT numbers for the chosen ROI.

CNR was described as:

$$CNR = \frac{X_S - X_W}{\sigma_{bg}} \quad (4)$$

where Xs, Xw are the average CT numbers of contrast agent and water, respectively and σbg is the quantity of image noise.

RESULTS

The measured CT numbers in the simulated CT system for water were 5±2, -1±1, -10±6, 0±3, 7±3, and 18±5 in the energy bin from 1 to 6, respectively. Overall, the percentage of the relative difference between simulated and experimental CT numbers of water was between 2% and less than 16% for 6 energy bins.

Fig 3, illustrates a cross-sectional image of both studied contrast agents (Fe_3O_4@Au, Fe_3O_4@Bi) in 2, 4, and 5 energy bins at a concentration of 4 mg/ml. According to Fig 3, the image quality of a given contrast agent varies at different energy bins. In bin 2, the image contrast of two contrast materials is approximately identical. CT numbers of Fe_3O_4@Au and Fe_3O_4@Bi nanocomposites in this bin are 96±5 and 94±12, respectively. As can be observed, Fe_3O_4@Au nanocomposites have higher CT numbers compared to Fe_3O_4@Bi nanocomposites, but these two CT numbers are slightly different and are not visible in images. In bin 4, image qualities of the contrast agent are different from bin 2 and 5. The image of Fe_3O_4@Au nanocomposites provides better contrast in comparison to Fe_3O_4@Bi nanocomposites in this energy range. In energy bin 4, the CT number of Fe_3O_4@Au is 144±10 and the CT number of Fe_3O_4@Bi is 130±18. Fe_3O_4@Au nanoparticles recorded an extremely higher CT number than Fe_3O_4@Bi in bin 4. However, in bin 5, the quality of reconstructed images is quite opposite of bin 4. In this energy bin, Fe_3O_4@Bi has produced a better quality compared to Fe_3O_4@Au. By comparing the CT number values of Fe_3O_4@Bi and Fe_3O_4@Au which are 162±19 and 135±4, respectively. Fe_3O_4@Bi has a higher CT number and therefore has a higher image quality than Fe_3O_4@Au in this energy range.

Fig 4, represents the signal intensity changes of Fe_3O_4@Au and Fe_3O_4@Bi contrast materials in 6 energy bins separately for each concentration. Also, the error bars in plots of Fig 4 indicate the standard deviation of CT numbers in the selected ROI. As the concentration of the contrast agent increases, the signal intensity in both studied contrast agents is amplified. As can be seen from Fig 4, in general, signal intensities of Fe_3O_4@Au and

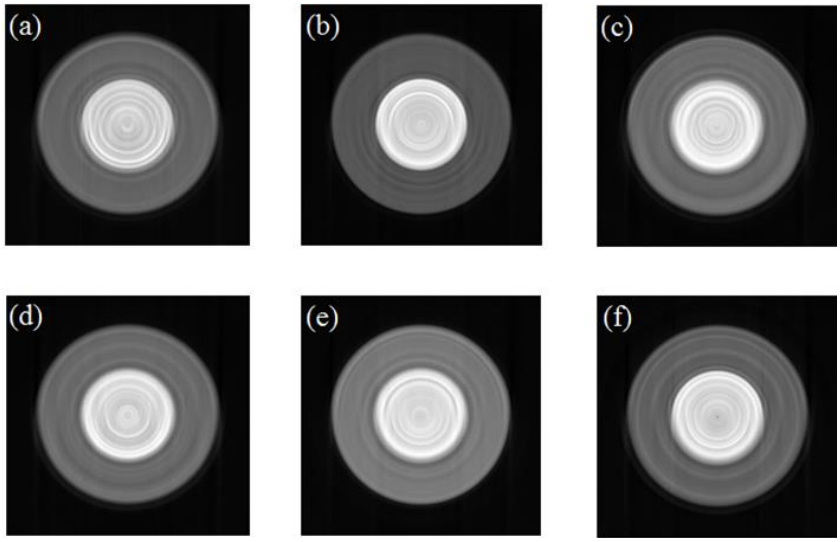

Fig 3. The first row is CT images of Fe_3O_4@Au nanocomposite. The second row is related to CT images of Fe_3O_4@Bi nanocomposite. (a) and (d) are CT images in the energy range of 20-40 Kev (bin 2). (b) and (e) are CT images in the energy range of 80-100 Kev (bin 4). (c) and (f) are CT images in the energy range of 100-120 Kev (bin5)

Fe_3O_4@Bi nanocomposites are slightly different from each other, except for bin 4 and 5, where this difference is more obvious. In both contrast agent, the signal intensity increases in the first two energy bins (bins 1 and 2), but decreases from the second energy bin onwards and reaches its lowest point in bin 3. Fe_3O_4@Au nanoparticles record the highest signal intensity in bin 4 and then have a downward trend in the final two bins (bin 5 and 6). Fe_3O_4@Bi nanoparticles from bin 3 had a trend of increasing CT number which continued up to bin 5 and showed the highest CT Number in this energy bin. However, the CT number in bin 6 is much lower than in bin 5 and is approximately equal to the CT number of Fe_3O_4@Au nanoparticles in this energy range. In this article, the highest CT numbers were measured for contrast agents at a concentration of 4 mg/ml. The highest CT number for Fe_3O_4@Au nanocomposites is in the 4th energy bin and is equal to 144±10 and for Fe_3O_4@Bi nanocomposites is in the 5th energy bin and is equal to 162±19. By comparing plots in Fig 4, increasing concentration from 0.5 to 4 mg/ml augments the signal intensity by 350% for gold nanocomposites and 288.8% for bismuth nanocomposites in bin 3.

The changes in CNR and their standard deviation for contrast agents in 6 energy bins at four studied concentrations are exhibited in Fig 5. Examination of graphs in Fig 5 indicates that as the concentration rises, the CNR of all contrast media enhances at all energy bins. According to Fig 5 and 6, the CNR of Fe_3O_4@Au nanocomposites

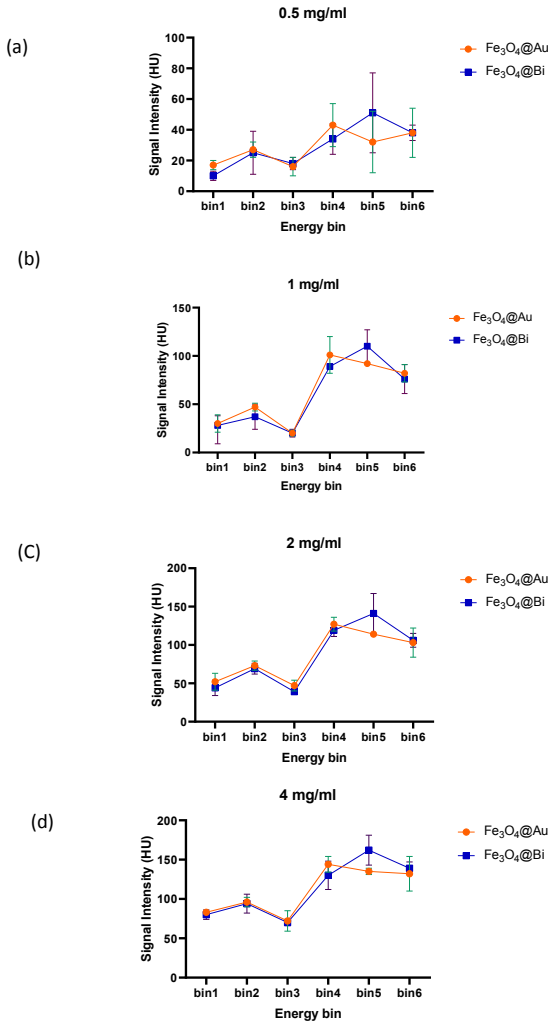

Fig 4. Signal intensity changes of tested contrast agents in various energy bins: (a) 0.5 mg/ml (b) 1 mg/ml and (c) 2 mg/ml (d) 4 mg/ml

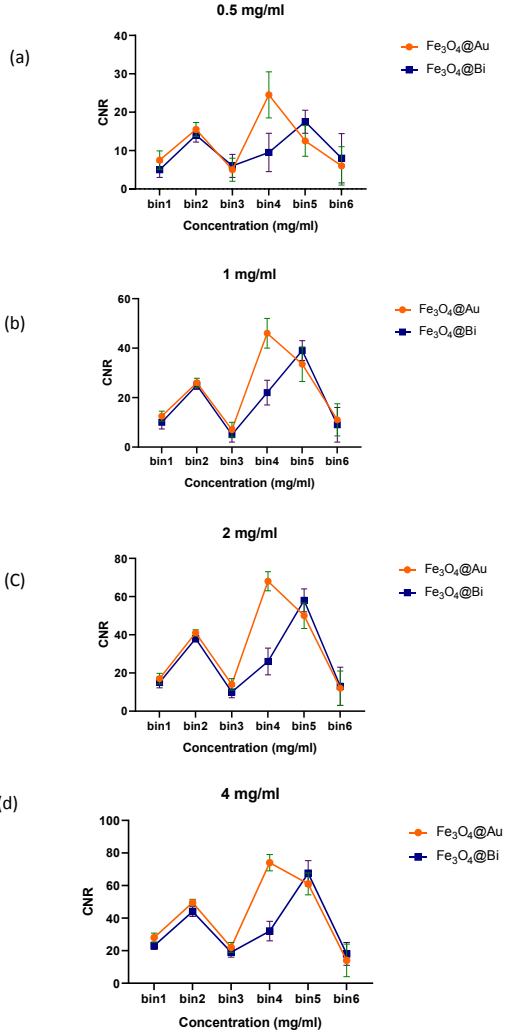

Fig 5. CNR variations for all contrast agents in 6 energy bins: (a) 0.5 mg/ml (b) 1 mg/mg (c) 2 mg/ml (d) 4 mg/ml

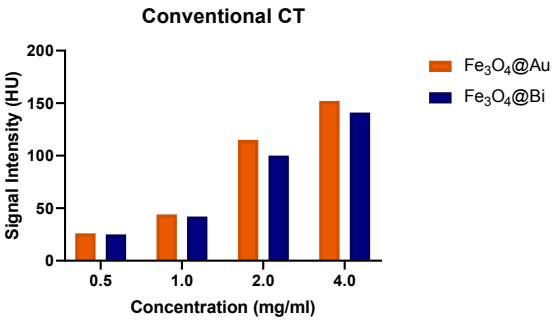

Fig 6. Comparison of CT numbers of Fe3O4@Au and Fe3O4@Bi hybrid nanocomposites at all tested concentrations in energy 140 kVp

increased in 1th and 2nd energy bin but decreased from 2th bin onwards, and in 3th bin reached the lowest level. After 3rd energy bin, the CNR values rise again and reach the highest level in the 4th bin then CNR drops in the 5th and 6th energy bin. Changing of CNR in terms of energy bin for Fe_3O_4@Bi nanocomposites similar to Fe_3O_4@Au nanocomposites in the first 3 energy bins but slightly different from 3rd bin onwards. After the 3rd bin, the CNR amount of bismuth nanocomposites increases, which continued until the 5th energy bin. During this energy range, it reaches its highest CNR level and then diminishes in the next energy bin. As can be seen from graphs, CNR values of two contrast agents at the same concentration in all energy bins are almost close to each other except bin 5 and 6. The maximum CNR of gold and bismuth nanocomposites was 74±6 in bin 4 and 67.5±9 in bin 5 at a concentration of 4 mg/ml, respectively. By switching concentration from 2 to 4 mg/ml, CNR grows 20.7% for Fe_3O_4@Au nanocomposites and 15.8% for Fe_3O_4@Bi nanocomposites in bin 2.

DISCUSSION

Generally, Fe_3O_4 nanoparticles are used as contrast media in MRI imaging. On the other hand, studies have shown that nanoparticles such as gold and bismuth are effective as contrast agents in CT imaging. Also, studies on the use of Fe_3O_4@Au nanocomposites as a multiple contrast agent in dual-mode MR/CT imaging have shown promising results. In this work, we designed Fe_3O_4@Au and Fe_3O_4@Bi hybrid nanocomposites and evaluated them by simulated spectral CT. The presented simulation outcomes demonstrated that signal intensity and CNR of images enhance by increasing the concentration of contrast agent. As the concentration rises, the number of nanoparticles in specified volume increases, so the amount of X-ray absorption goes up, which in turn grows signal intensity and CNR.

Moreover, results showed that Fe_3O_4@Au and Fe_3O_4@Bi hybrid nanocomposites produced nearly similar image quality except in the energy range of 80 to 120 keV. As we know from radiation physics, gold and bismuth have linear attenuation coefficients that are nearly similar at different energies. Although in the energy range of about 80 to 100 keV, the discrepancy in attenuation coefficients between two materials has increased dramatically. This discrepancy is due to the presence of K edges of gold and bismuth, which are located in this energy range. The K-edge happens at photon energy 80.7 keV for gold and 90.5 keV for bismuth. Therefore, the signal intensity of Fe_3O_4@Au nanocomposites increased sharply in the 4th energy bin and was much higher than the signal intensity of Fe_3O_4@Bi nanocomposites, and after this energy bin, signal intensities diminish again. As well as, bismuth hybrid nanocomposite recorded the most signal intensity in bin 5, which is due to the higher linear attenuation coefficient of this material in this energy range.

To the best of our knowledge, no studies related to the application of Fe_3O_4@Au and Fe_3O_4@Bi hybrid nanocomposites in spectral CT were found to compare with our results. Therefore, conventional CT information obtained in the simulated scanner was reported for better comparison. Fig 6 shows the signal intensity of both contrast agents in terms of different concentrations. These data were obtained from conventional CT at the peak energy of 140 kVp. Our results indicated that the signal intensity of all studied hybrid nanocomposites is concentration-dependent and augments with increasing concentration of the contrast material. If we compare our results with other similar studies, our results were in agreement with Li et al [38] and Motiei et al [42]. In both of these studies, the properties of Fe_3O_4@Au nanoparticles were investigated in medical imaging. They found that with increasing concentration, the signal intensity of Fe_3O_4@Au nanoparticles increases linearly. Although the results of this work show slight discord in measured CT numbers with reported results in the article by Wang et al [40], this difference may be due to differences in nanocomposite composition and variation in energy spectrum or differences in

CT scanner used.

By assessing the results of Fe_3O_4@Bi nanocomposites with related studies, the results of the present study were in accordance with Veintemillas-Verdaguer et al [43]. They proved that core-shell iron oxide bismuth oxide nanocomposite offers promising results as a multiple contrast agent in CT and MRI imaging. Higher X-ray absorption of bismuth causes better contrast in CT images. However, there is some discrepancy between the results of our CT numbers and their reported values. This could be due to differences in the composition of nanocomposite as well as the specifications of CT scanner including differences in voltage, image reconstruction method, and detector performances. However, the CT numbers results of our study differed partly from the findings of Lou et al [44]. This discordance is related to the difference in composition of nanoparticles used in these studies so that in the study of Lou et al, Fe_3O_4@polydopamine (PDA)@bovine serum albumin (BSA)-Bi2S3 composite was used.

CONCLUSION

In summary, we simulated Fe_3O_4@Au and Fe_3O_4@Bi nanocomposites as multifunction nanoparticles contrast agents and evaluated their imaging properties by spectral CT. Our results proved that Fe_3O_4@Au and Fe_3O_4@Bi nanocomposites produced almost the same image quality. However, in the energy range of 80 to 120 keV, the difference between these two nanocomposites has increased so that Fe_3O_4@Au nanoparticles in the energy range of 80 to 100 keV had a higher signal intensity and CNR than Fe_3O_4@Bi and also Fe_3O_4@Bi nanoparticles in the energy range of 100 to 120 keV produced better imaging properties. Moreover, our results indicated that the signal intensity and CNR of nanocomposites depend on the concentration so that the maximum CT number and CNR are observed at the highest studied concentration. Fe_3O_4@Bi nanocomposite could be a better option in comparison to Fe_3O_4@Au nanocomposite due to its lower price and availability.

Overall, Fe_3O_4@Au and Fe_3O_4@Bi nanocomposites are promising contrast agents in medical imaging and are recommended for in vivo animal preclinical experiments and follow up on future clinical trials.

ACKNOWLEDGMENTS

The project was supported by the Medical Radiation Sciences Research Team and the Medical Physics department of Tabriz University of Medical Sciences.

REFERENCES

1. Mahan MM, Doiron AL. Gold nanoparticles as x-ray, CT, and multimodal imaging contrast agents: formulation, targeting, and methodology. J Nanomater. 2018; 2018: 5837276.
2. kavousi z, Karimian A, Jabbari I. Assessment of x-ray crosstalk in a computed tomography scanner with small detector elements using Monte Carlo method. IJMP. 2018; 15(3): 169-175.
3. Chen J, Yang XQ, Qin MY, Zhang XS, Xuan Y, Zhao YD. Hybrid nanoprobes of bismuth sulfide nanoparticles and CdSe/ZnS quantum dots for mouse computed tomography/fluorescence dual mode imaging. J Nanobiotechnology. 2015; 13: 76.
4. Mullner M, Schlattl H, Hoeschen C, Dietrich O. Feasibility of spectral CT imaging for the detection of liver lesions with gold-based contrast agents - a simulation study. Phys Med. 2015; 31(8): 875-881.
5. Van Ommen F, Bennink E, Vlassenbroek A, Dankbaar JW, Schilham AMR, Viergever MA, et al. Image quality of conventional images of dual-layer spectral CT: a phantom study. Med Phys. 2018; 45(7): 3031-3042.
6. Si-Mohamed S, Bar-Ness D, Sigovan M, Tatard-Leitman V, Cormode DP, Naha PC, et al. Multicolour imaging with spectral photon-counting CT: a phantom study. Eur Radiol Exp. 2018; 2(1): 34.
7. Jo BD, Park SJ, Kim HM, Kim DH, Kim HJ. Spectral computed tomography for quantitative decomposition of vulnerable plaques using a dual-energy technique: a Monte Carlo simulation study. J Instrum. 2016; 11(02): P02011-P.
8. Kim J, Bar-Ness D, Si-Mohamed S, Coulon P, Blevis I, Douek P, et al. Assessment of candidate elements for development of spectral photon-counting CT specific contrast agents. Sci Rep. 2018; 8(1): 12119.
9. Willemink M, Persson M, Pourmorteza A, Pelc N, Fleischmann D. Photon-counting CT: technical principles and clinical prospects. Radiol Artif Intell. 2018; 289: 172656.
10. Badea CT, Clark DP, Holbrook M, Srivastava M, Mowery Y, Ghaghada KB. Functional imaging of tumor vasculature using iodine and gadolinium-based nanoparticle contrast agents: a comparison of spectral micro-CT using energy integrating and photon counting detectors. Phys Med Biol. 2019; 64(6): 065007.
11. Amato C, Klein L, Wehrse E, Rotkopf LT, Sawall S, Maier J, et al. Potential of contrast agents based on high-Z elements for contrast-enhanced photon-counting computed tomography. Med Phys. 2020.
12. Tao S, Rajendran K, McCollough CH, Leng S. Feasibility of multi-contrast imaging on dual-source photon counting detector (PCD) CT: An initial phantom study. Med Phys. 2019.
13. Boussel L, Coulon P, Thran A, Roessl E, Martens G, Sigovan M, et al. Photon counting spectral CT component analysis of coronary artery atherosclerotic plaque samples. Br J Radiol. 2014; 87(1040): 20130798.
14. Pelc NJ, Glick SJ, Samei E, Didier CS, Nishikawa RM. The

effect of characteristic x-rays on the spatial and spectral resolution of a CZT-based detector for breast CT. Medical Imaging 2011: Physics of Medical Imaging 2011.
15. Jo B, Im HS, Kim HJ, Son TJ. The potential of spectral-CT for material decomposition with gold-nanoparticle and iodine contrast. 2015; 51: 22-25.
16. Lu G, Marsh S, Damet J, Carbonez P, Laban J, Bateman C, et al. Dosimetry in MARS spectral CT: TOPAS Monte Carlo simulations and ion chamber measurements. Australas Phys Eng Sci Med. 2017; 40(2): 297-303.
17. Sun IC, Eun DK, Na JH, Lee S, Kim IJ, Youn IC, et al. Heparin-coated gold nanoparticles for liver-specific CT imaging. Chemistry. 2009; 15(48): 13341-13347.
18. Karunamuni R, Tsourkas A, Maidment AD. Exploring silver as a contrast agent for contrast-enhanced dual-energy X-ray breast imaging. Br J Radiol. 2014; 87(1041): 20140081.
19. Kang S, Eom J, Kim B, Lee S. Evaluation of gold K-edge imaging using spectral computed tomography with a photon-counting detector: A Monte Carlo simulation study. Optik. 2017; 140: 253-260.
20. Lusic H, Grinstaff MW. X-ray-computed tomography contrast agents. Chem Rev. 2013; 113(3): 1641-1666.
21. Rathnayake S, Mongan J, Torres AS, Colborn R, Gao DW, Yeh BM, et al. *In vivo* comparison of tantalum, tungsten, and bismuth enteric contrast agents to complement intravenous iodine for double-contrast dual-energy CT of the bowel. Contrast Media Mol Imaging. 2016; 11(4): 254-261.
22. Ghadiri H, Ay MR, Shiran MB, Soltanian-Zadeh H, Zaidi H. K-edge ratio method for identification of multiple nanoparticulate contrast agents by spectral CT imaging. Br J Radiol. 2013; 86(1029): 20130308.
23. Chhour P, Naha PC, Cheheltani R, Benardo B, Mian S, Cormode DP. Gold nanoparticles for biomedical applications: synthesis and *in vitro* evaluation. Nanomaterials in Pharmacology: Springer; 2016. p. 87-111.
24. Sadeghian M, Akhlaghi P, Mesbahi A. Investigation of imaging properties of novel contrast agents based on gold, silver and bismuth nanoparticles in spectral computed tomography using Monte Carlo simulation. PJMPE. 2020; 26: 21-29.
25. Xi D, Dong S, Meng X, Lu Q, Meng L, Ye J. Gold nanoparticles as computerized tomography (CT) contrast agents. RSC Adv. 2012; 2(33): 12515-12524.
26. Dehghani S, riyahi alam N, Shahriarian S, Mortezazadeh T, Haghgoo S, Golmohamadpour A, et al. The effect of size and aspect ratio of Fe-MIL-88B-NH2 metal-organic frameworks on their relaxivity and contrast enhancement properties in MRI: *in vitro* and *in vivo* studies. J Nanopart Res. 2018; 20.
27. Mansouri H, Gholibegloo E, Mortezazadeh T, Yazdi MH, Ashouri F, Malekzadeh R, et al. A biocompatible theranostic nanoplatform based on magnetic gadolinium-chelated polycyclodextrin: *in vitro* and *in vivo* studies. Carbohydr Polym. 2021; 254: 117262.
28. Cole L, Ross R, Tilley J, Vargo-Gogola T, Roeder R. Gold nanoparticles as contrast agents in X-ray imaging and computed tomography. Nanomedicine (Lond). 2015; 10: 321-341.
29. Cormode DP, Skajaa T, van Schooneveld MM, Koole R, Jarzyna P, Lobatto ME, et al. Nanocrystal core high-density lipoproteins: a multimodality contrast agent platform. Nano lett. 2008; 8(11): 3715-3723.
30. Dong YC, Hajfathalian M, Maidment PSN, Hsu JC, Naha PC, Si-Mohamed S, et al. Effect of gold nanoparticle size on their properties as contrast agents for computed tomography. Sci Rep. 2019; 9(1): 14912.
31. Li C-H, Kuo T, Su H-J, Lai W-Y, Yang P-C, Chen J-S, et al. Fluorescence-guided probes of aptamer-targeted gold nanoparticles with computed tomography imaging accesses for *in vivo* tumor resection. Sci Rep. 2015; 5: 15675.
32. Mortezazadeh T, Gholibegloo E, Khoobi M, Alam NR, Haghgoo S, Mesbahi A. *In vitro* and *in vivo* characteristics of doxorubicin-loaded cyclodextrine-based polyester modified gadolinium oxide nanoparticles: a versatile targeted theranostic system for tumour chemotherapy and molecular resonance imaging. J Drug Target. 2020; 28(5): 533-546.
33. Sanchez LM, Alvarez VA. Advances in magnetic noble metal/iron-based oxide hybrid nanoparticles as biomedical devices. Bioengineering (Basel). 2019; 6(3): 75.
34. Cai H, Li K, Shen M, Wen S, Luo Y, Peng C, et al. Facile assembly of Fe_3O_4@Au nanocomposite particles for dual mode magnetic resonance and computed tomography imaging applications. J Mater Chem. 2012; 22: 15110-15120.
35. Dheyab MA, Aziz AA, Jameel MS, Noqta OA, Mehrdel B. Synthesis and coating methods of biocompatible iron oxide/gold nanoparticle and nanocomposite for biomedical applications. Chin J Phys. 2020; 64: 305-325.
36. Lee N, Yoo D, Ling D, Cho MH, Hyeon T, Cheon J. Iron oxide based nanoparticles for multimodal imaging and magnetoresponsive therapy. Chem Rev. 2015; 115(19): 10637-10689.
37. Pariti A, Desai P, Maddirala SKY, Ercal N, Katti K, Liang X, et al. Superparamagnetic Au-Fe_3O_4 nanoparticles: one-pot synthesis, biofunctionalization and toxicity evaluation. Mater Res Express. 2014; 1: 035023.
38. Li J, Zheng L, Cai H, Sun W, Shen M, Zhang G, et al. Facile one-pot synthesis of Fe_3O_4@Au composite nanoparticles for dual-mode MR/CT imaging applications.ACS Appl Mater Interfaces. 2013; 5(20): 10357-10366.
39. Narayanan S, Sathy BN, Mony U, Koyakutty M, Nair SV, Menon D. Biocompatible magnetite/gold nanohybrid contrast agents via green chemistry for MRI and CT bioimaging. ACS Appl Mater Interfaces. 2012; 4(1): 251-260.
40. Wang G, Gao W, Zhang X, Mei X. Au nanocage functionalized with Ultra-small Fe_3O_4 nanoparticles for targeting T1–T2Dual MRI and CT imaging of tumor. Sci Rep. 2016; 6: 28258.
41. Pelowitz DB: MCNPX user's manual version (2.6.0).; Los Alamos National Laboratory. 2008.
42. Motiei M, Dreifuss T, Sadan T, Omer N, Blumenfeld-Katzir T, Fragogeorgi E, et al. Trimodal nanoparticle contrast agent for CT, MRI and SPECT imaging: synthesis and characterization of radiolabeled core/shell iron oxide@ gold nanoparticles. Chem Lett. 2019; 48: 291-294.
43. Veintemillas-Verdaguer S, Luengo Y, Serna C, Vergés M, Varela M, Calero M, et al. Bismuth labeling for the CT assessment of local administration of magnetic nanoparticles. Nanotechnology. 2015; 26: 135101.
44. Luo K, Zhao J, Jia C, Chen Y, Zhang Z, Zhang J, et al. Integration of Fe_3O_4 with Bi2S3 for multi-modality tumor theranostics. ACS Appl Mater Interfaces. 2020; 12(20): 22650-22660.